

Unsteady drag following shock wave impingement on a dense particle curtain measured using pulse-burst PIV

Edward P. DeMauro,^{*} Justin L. Wagner,[†] Steven J. Beresh,[‡] and Paul A. Farias
*Sandia National Laboratories, Engineering Sciences Center, P.O. Box 5800, MS-0825,
 Albuquerque, New Mexico 87185, USA*

(Received 23 September 2016; revised manuscript received 9 March 2017; published 8 June 2017)

High-speed, time-resolved particle image velocimetry with a pulse-burst laser was used to measure the gas-phase velocity upstream and downstream of a shock wave–particle curtain interaction at three shock Mach numbers (1.22, 1.40, and 1.45) at a repetition rate of 37.5 kHz. The particle curtain was formed from free-falling soda-lime particles resulting in volume fractions of 9% or 23% at mid-height, depending on particle diameter (106–125 and 300–355 μm , respectively). Following impingement by a shock wave, a pressure difference was created between the upstream and downstream sides of the curtain, which accelerated flow through the curtain. Jetting of flow through the curtain was observed downstream once deformation of the curtain began, demonstrating a long-term unsteady effect. Using a control volume approach, the unsteady drag on the curtain was estimated from velocity and pressure data. The drag imposed on the curtain has a strong volume fraction dependence with a prolonged unsteadiness following initial shock impingement. In addition, the data suggest that the resulting pressure difference following the propagation of the reflected and transmitted shock waves is the primary component to curtain drag.

DOI: [10.1103/PhysRevFluids.2.064301](https://doi.org/10.1103/PhysRevFluids.2.064301)

I. INTRODUCTION

An understanding of the complex physics associated with the interaction of a shock wave with a multiphase mixture is important in many engineering applications, such as pulsed detonation engines [1,2], mining safety [3], rocket propulsion [4], and explosive dispersion of heterogeneous mixtures [5]. When a shock wave interacts with a multiphase mixture, momentum and energy are exchanged between the phases. Oftentimes, these interactions involve clouds or agglomerations of solid or liquid particles, where the momentum and energy exchange are not readily understood. The difficulty therefore arises in that the interparticle interactions (collisions) and the aerodynamics of the particles in the presence of a highly compressible flow (i.e., drag) combine to make accurate predictions difficult [6]. In addition, the aerodynamic behavior of a dense gas-solid mixture cannot be extrapolated from that of isolated particles due to the non-negligible influence of volume fraction.

A gas-solid mixture may be divided into one of three categories based on volume fraction (φ_p): dilute ($\varphi_p < 1\%$), granular ($50\% < \varphi_p$), and an intermediate, dense gas-solid regime in the range $1\% \leq \varphi_p \leq 50\%$ [5]. In this sense, dilute mixtures form an extreme where the volume of the solid particles is negligible in relation to the volume of the gas, such as a fine dust. In comparison, granular mixtures contain solid particle volumes that are greater than or equal to the volume of fluid within the mixture. In these mixtures, interactions between the particles cannot be neglected, as the particles are, in fact, in direct contact with each other [5]. Finally, dense mixtures are those in which the solid volume is non-negligible, but the particles are not in constant contact with each other.

^{*}Current address: Rutgers, The State University of New Jersey, 98 Brett Road, Room D102, Piscataway, New Jersey 08854, USA; edward.demauro@rutgers.edu

[†]jwagner@sandia.gov

[‡]sjberes@sandia.gov

A variety of studies has been performed to model or directly measure the interaction of a shock wave with a dilute gas-solid mixture, with many of these modeling efforts summarized by Marble [7]. Within the literature, estimation of the drag imposed on a multiphase mixture following impingement by a shock wave has provided difficulties for a variety of reasons. It has been established for some time that the standard drag law underpredicts the drag imposed on dilute flows. Rudinger [6] first noted difficulty in the standard drag model's prediction of the dispersal of particles within a dusty cloud, a finding echoed by Sommerfeld [8], who noted that many researchers simply create a drag law suitable strictly for their own data set. One major problem presented in the standard drag law is that it relates the drag coefficient strictly to an empirical function of the diameter-based Reynolds number. In contrast, many other terms have been identified as contributing to the overall drag imposed on a dilute flow; these include quasisteady, inviscid, and lift forces [9,10] as well as compressibility influences [11].

Many studies have been performed in order to correctly model particle drag by improving assumptions associated with compressibility and unsteadiness effects [10,12–14]. Parmar *et al.* [10] developed a model, validated with experimental work from Britan *et al.* [15], Sun *et al.* [12], and Skews *et al.* [16], which showed that unsteady loading was largely limited to the transient associated with a shock wave passing over a given particle, quickly dissipating to negligible values thereafter. Furthermore, their study concluded that drag measurements tended to rapidly asymptote towards quasisteady predictions. Wagner *et al.* [11] demonstrated that unsteady drag did not appear to contribute to long-time drag behavior in dilute gas-solid mixtures; rather, the particle drag showed a strong Mach number dependence, in agreement with the work of Loth [13] and Parmar *et al.* [10].

In comparison to dilute particle mixtures, little work has been performed on dense gas-solid mixtures. The works of Boiko *et al.* [17] and Rogue *et al.* [18] provide two early investigations into dense gas-solid particle regimes. Rogue *et al.* [18], for example, noted that interaction with these mixtures results in the creation of a transmitted shock wave that continues to propagate downstream through the mixture, and a reflected shock that travels back upstream of the mixture, which was also seen by Boiko *et al.* [17] for their larger volume fractions. Outside of these, however, investigations of the dispersal of dense gas-solid mixtures as a whole, and its drag in particular, are limited in comparison to the dilute regime.

The question of particle dispersion in the dense gas-solid regime requires a definition of the major contributors to the imposed drag. Experimental work performed by Wagner *et al.* [19,20] on the interaction of a shock wave with a dense gas-solid mixture provides some insight into the dispersal mechanism. These tests were performed on a particle curtain formed of soda-lime particles with a diameter of 106–125 μm , resulting in a volume fraction of 20%. From high-speed Schlieren and unsteady pressure measurements, they were able to observe the formation of a reflected and transmitted shock wave emanating from the curtain postinteraction with the shock wave, similar to what was seen by Boiko *et al.* [17] and Rogue *et al.* [18], along with spreading of the particle curtain in the streamwise direction [19]. Furthermore, recent x-ray measurements by Wagner *et al.* [20] have shown particle drag during the interaction to exceed quasisteady drag predicted by Parmar *et al.* [10].

Using the data from Wagner *et al.* [19], Ling *et al.* [21] developed a new drag law model that incorporated drag unsteadiness, the influence of compressibility on drag, volume fraction influences, and interparticle interaction effects, which better reproduced the behavior of dense gas-solid mixtures seen in the experiments of Wagner *et al.* [19]. Other studies have also been performed to improve upon estimation of the dense mixture drag [22–24]; however, more data is required to refine these estimates and broaden their applicability [21]. To this end, additional shock tube investigations of dense mixture interactions include Kellenberger *et al.* [25] and the work of Theofanous *et al.* [26], which focused on scaling relationships in the dense regime.

The work presented here is a continuation of the work shown in Wagner *et al.* [19,20], making use of a pulse-burst laser to produce time-resolved particle image velocimetry (TR-PIV) measurements of the gas-phase velocity upstream and downstream of the particle curtain, following interaction with a planar shock wave. The results of these measurements, along with unsteady pressures, are

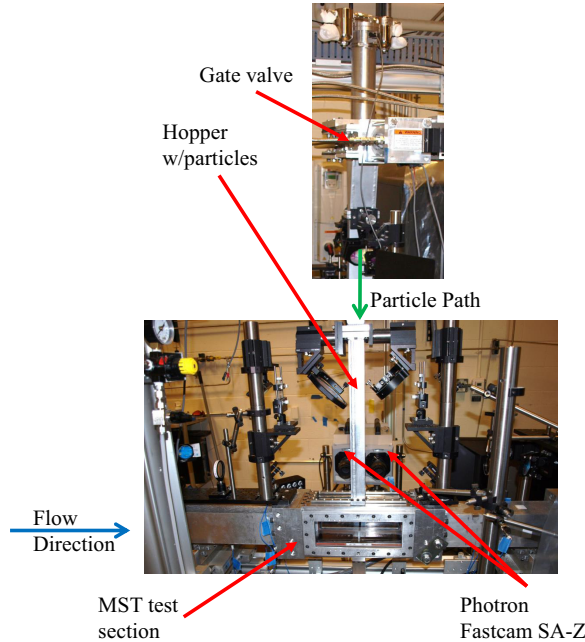


FIG. 1. The multiphase shock tube (MST) with relevant sections identified.

then used to perform a control volume analysis, which estimates the total unsteady drag imposed on the dense gas-solid mixture as a function of time. In this sense, this study endeavors to measure the unsteady drag imposed on the dense mixture and provide further insight into the mechanism of particle dispersal and its relationship to the better understood single-particle drag.

II. EXPERIMENTAL SETUP

A. Multiphase shock tube

The multiphase shock tube (MST) is shown in Fig. 1. The driver section of the shock tube was constructed from a 2.1-m-long stainless steel pipe with an inner diameter of 89 mm, supplied with a high pressure nitrogen source. The driven section consists of square tubing, 5.2 m long, with an inner width of $H = 76$ mm. The driven gas was air at an initial temperature and absolute pressure of 300 K and 84.1 kPa, respectively.

In lieu of burst discs, a Dynamics Systems Research (Model 183–1.5–2000) fast-acting valve was used to fire the shock tube due to its repeatability and comparably rapid turn-around time. It has been shown that this valve is capable of producing flow conditions comparable to those achieved from a traditional burst disk setup [27].

Experiments were conducted at three shock Mach numbers: $M_s = 1.22, 1.40,$ and 1.45 (based on time of arrival of the shock wave at the pressure transducers), which corresponded to driver pressures of 690, 2070, and 2760 kPa. Prior to an experiment, soda-lime particles rested on an initially closed gate valve located above the test section of the shock tube. The experiments presented here were performed using two separate diameter distributions (d_p): 106–125 and 300–355 μm . When the gate valve was opened, particles under the influence of gravity flowed through a beveled 3.2 mm slit in the test section ceiling, forming a particle curtain measuring (initially) $\delta_0 = 1.5 \pm 0.2$ or 3.5 ± 0.2 mm in streamwise thickness at mid-height, depending on particle diameter distribution. Even though the slit was held constant, two different thicknesses arose due to the change in particle diameter. The particle curtain was measured to flow at an average rate (within 95% confidence) of 56.0 ± 0.24

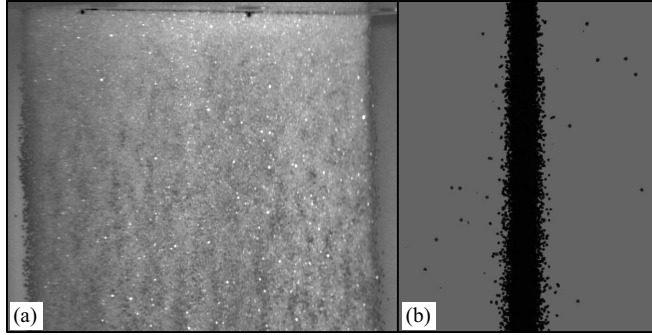


FIG. 2. (a) Instantaneous image of the particle curtain ($d_p = 300\text{--}355\ \mu\text{m}$) obtained at an oblique angle; (b) instantaneous side view of the particle curtain used to measure the curtain thickness.

and $52.6 \pm 0.23\ \text{g/s}$, for the $d_p = 106\text{--}125$ and $300\text{--}355\ \mu\text{m}$ curtains, respectively. Note that all uncertainties presented herein are with respect to the mean. Before firing the shock tube, the particle curtain flowed through the test section for a second to ensure that the steady state had been reached within the curtain. The particles exited the test section through a similar slit in the floor, where they entered a collection reservoir.

B. Characterization of the particle curtain prior to shock arrival

An extensive set of tests was conducted to characterize and quantify the particle curtain, including measurements of the particle velocity, mass flow rate, and curtain thickness. Assuming a constant cross-sectional area A_c , the density of the particle curtain as a function of height y can be shown to be

$$\rho_{\text{mix}}(y) = \frac{\dot{m}_{\text{mix}}}{u_p(y)A_c}, \quad (1)$$

where u_p is the velocity of the particles, \dot{m}_{mix} is the mass flow rate of the mixture, and the subscript “mix” refers to properties pertaining to the gas-solid mixture. The particles were observed to free fall at an average velocity of $0.89\ \text{m/s}$ at mid-height; therefore they were essentially frozen in comparison to the shock velocities. From this, it was shown that a simple free-fall equation could be used to model the velocity of the particles, i.e., $u_p(y) \approx \sqrt{2g(H/2 - y)}$, where the particle velocity was taken to be nearly zero at the entrance slit into the shock tube test section. Because the volume fraction (φ_p) varies across the height of the particle curtain, it was defined as that measured at mid-height, determined from

$$\varphi_p = \frac{\forall_p}{\forall_{\text{mix}}} = \frac{\rho_{\text{mix}} - \rho_{\text{air}}}{\rho_p - \rho_{\text{air}}}, \quad (2)$$

where \forall is volume and ρ is density; in Eq. (2), the subscripts “p” and “air” indicate quantities pertaining to the particles and air, respectively.

Figure 2 shows an image of the particle curtain ($d_p = 300\text{--}355\ \mu\text{m}$), acquired at an oblique angle, along with a shadowgraph image of the curtain used to measure the thickness. Note that a background subtraction was performed in both images to highlight relevant features. Under the assumption of a uniform particle distribution, φ_p was measured to be $\sim 23 \pm 3\%$ and $\sim 9 \pm 0.5\%$ at the center of the curtain ($106\text{--}125$ and $300\text{--}355\ \mu\text{m}$ particles, respectively), where the ranges correspond to uncertainties associated with the curtain mass flow rate and thickness. For the remainder of the paper, the particle curtain will be referred to by the associated value of φ_p . Within Fig. 2(a), gaps become apparent within the particle curtain. The curtain shown here is $\varphi_p = 9\%$; therefore the nonuniformity is associated with the volume fraction decreasing closer to the floor of the shock tube. Note that in

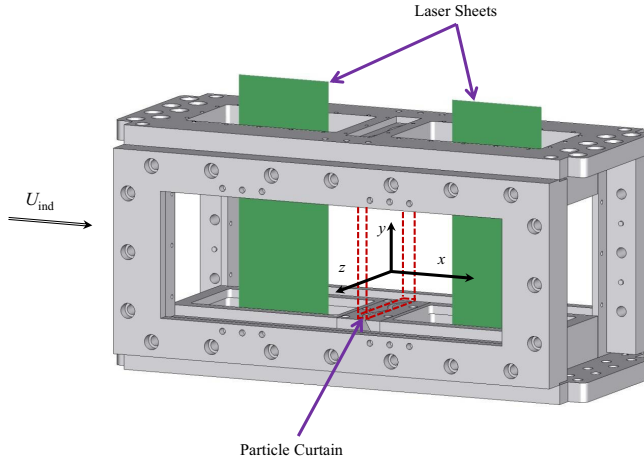


FIG. 3. Schematic of the experimental setup with axis orientation, including upstream and downstream locations of TR-PIV measurements. The coordinate system is defined such that the origin is at mid-height and mid-thickness of the particle curtain (indicated by the red dotted outline).

reality, the curtain initially has a streamwise Gaussian particle distribution [20,22,28]; however, for purposes of simplicity, this was assumed to be a negligible factor.

C. Experimental measurement procedure

1. Pulse-burst PIV

Previous PIV realizations in shock tubes have typically been difficult due to low repetition rates, allowing for only a single realization to be obtained in the millisecond test times of a shock tube [29–32]. Recent advances and the commercialization of pulse-burst laser technology, however, have made time-resolved PIV (TR-PIV) in high-speed flows a feasible and attractive option to overcome this limitation [27,33]. For this study, the light source for the TR-PIV was a Quasi-Modo (Spectral Energies, LLC) burst-mode laser, with a maximum repetition rate of 500 kHz, which provided ~ 25 mJ per pulse at 37.5 kHz at 532 nm. The duration of the burst was 10.2 ms, greater than the typical test times in the MST (about 1 ms), with each pulse width lasting 6 ns. The laser was operated in a doublet (i.e., double pulsed) mode, where the time delay between pulses was set to $\Delta t = 4 \mu\text{s}$ for maximum displacements of one-third the interrogation window.

Typical sheet-forming optics were used to shape the laser into two separate 1.5-mm-thick laser sheets, as seen in Fig. 3, to provide for simultaneous measurement of upstream and downstream fields of view. The laser sheets were positioned at the spanwise center plane of the shock tube test section. A beam splitter was used to form two sheets to allow for the regions upstream and downstream of the curtain to be measured simultaneously. Two Photron SA-Z cameras, each with a maximum resolution of 1024×1024 digitized to 12 bits, were set to a resolution of 680×340 pixels at 75 kHz, in order to frame straddle the 37.5 kHz doublets. Images were acquired using a pair of 105 mm camera lenses, which were set to $f/11$.

Seed particles were produced from mineral oil using a TSI six-jet atomizer, and were introduced into the shock tube about 0.5 m downstream of the fast-acting valve. *In situ* measurements showed that the atomizer delivered a particle size of $\sim 1.6 \mu\text{m}$; this resulted in Stokes numbers ranging from 0.025–0.06, depending on flow conditions. At these Stokes numbers, the seed particles are expected to faithfully track the flow [34]. These smoke particles were introduced into the driven section before a run, with particle delivery terminated prior to firing the shock tube; therefore, there was negligible seed velocity prior to initiation of a test.

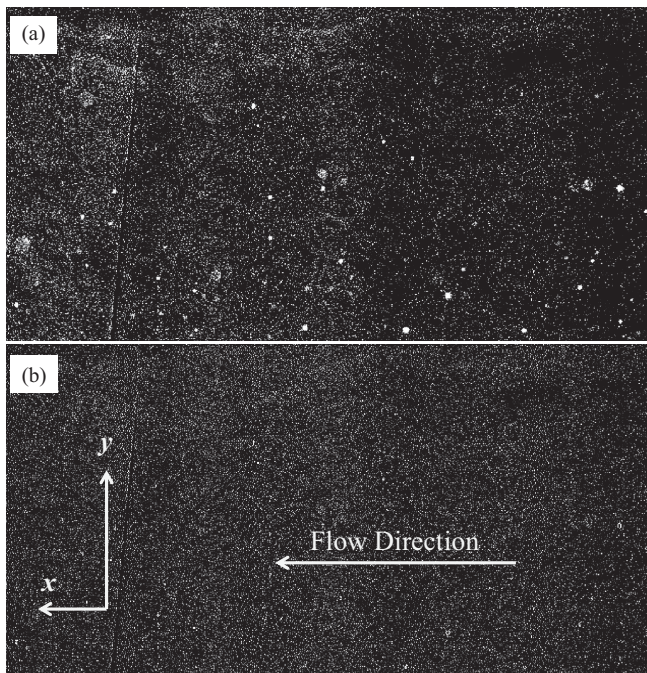


FIG. 4. Examples of raw and preprocessed seeded images, $\varphi_p = 9\%$: (a) larger soda-lime particles are present within the image; (b) the same image passed through a Fourier high-pass filter with the intensity associated with larger particles attenuated.

Raw images were preprocessed using a Fourier high-pass filtering technique, described in Sec. II C 2. Vector fields were processed with the LaVision Davis 8.3 software package using a multipass method, with an initial interrogation window size of 64×64 pixels with 50% overlap, followed by two iterations performed with an interrogation window size of 32×32 pixels at a 75% overlap. A Gaussian weighting function was applied to the interrogation windows. Spurious vectors associated with soda-lime particle light scattering were removed using a vector range filter as the soda-lime particles move much slower than the gas flow that carries the PIV particles; remaining errors were addressed with a median filter with a 5×5 spatial universal outlier detector. As can be seen in Fig. 2(b), extraneous particles were found to propagate upstream and downstream of the curtain, away from the core curtain flow, entering the associated fields of view. While vector validation was used to decrease the influence of the soda-lime particles on the processed vector fields, it was first necessary to apply an image filter to the raw images to further mitigate their effect on the processed vector fields.

2. Image filter

Due to the proximity of the two fields of view to the particle curtain, soda-lime particles from the curtain were at times evident in either field of view. These were particles that randomly fell outside of the bulk motion of the curtain, whether upon startup [Fig. 2(b)] or later displaced downstream once the curtain began to deform (Fig. 6). This can be seen in Fig. 4(a), where larger particles indicate the presence of soda lime within the seeded raw image. The raw and filtered image corresponds to a location upstream of the particle curtain; coordinate axes (with an arbitrary origin) are placed to indicate the streamwise and wall-normal directions. In order to mitigate the presence of spurious vectors associated with slower-moving soda-lime particles, a high-pass filter was applied to all images prior to processing, removing spatial frequencies up to $\sim 0.2 \text{ mm}^{-1}$. This was accomplished

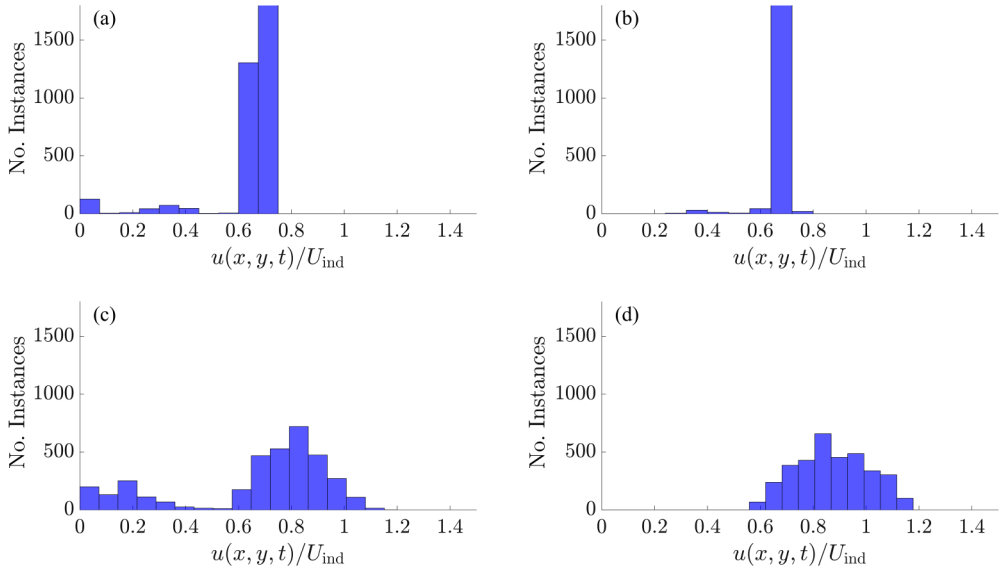


FIG. 5. Example histograms comparing vector fields processed (a), (c) from raw, unfiltered images and (b), (d) from filtered images for (a), (b) upstream and (c), (d) downstream fields of view. This figure corresponds to $M_s = 1.45$, $\varphi_p = 23\%$, at time $t^* = 78.2$.

by performing a convolution of the raw image files [35,36]. An example of a filtered image can be seen in Fig. 4(b), where the presence of the larger soda-lime particles has been greatly attenuated. This method is in contrast to the procedure performed by Zhang *et al.* [37], who used a type of algorithmic mask to remove larger particles from seeded images.

To better illustrate the effectiveness of the Fourier filter, example histograms are presented in Fig. 5, corresponding to $M_s = 1.45$ ($\varphi_p = 23\%$), for a time following passage of the reflected or transmitted shock waves. This case was chosen to illustrate the effectiveness of the filter in that the downstream field of view for this case saw the intrusion of a large number of soda-lime particles that resulted in spurious vector calculations. The histograms associated with unfiltered data demonstrate the presence of slower-speed realizations within the processed vector fields, which are greatly attenuated in the filtered data. For this reason, the data presented in the subsequent sections were preprocessed using the Fourier high-pass filter.

A few interesting features are to be noticed in the sample histograms shown in Fig. 5. Within the upstream field of view [Figs. 5(a) and 5(b)], the filter attenuates realizations less than $0.5U_{\text{ind}}$. The effect seen here is to narrow the variance of the histogram and increase the number of instances measured at $\sim 0.7U_{\text{ind}}$. In comparison, within the downstream field of view [Figs. 5(c) and 5(d)], instances less than $0.5U_{\text{ind}}$ have once again been removed; however, the effect is an increase in the variance within the downstream histogram [Fig. 5(d)], where measured values of velocity can be seen to reach as high as $\sim 1.1U_{\text{ind}}$. In other words, inaccurate velocity realizations have been replaced with high-velocity vectors now measurable with the high-pass filter. As will be discussed in Sec. III B, this corresponds to resolving jetting of accelerated velocity that can be seen developing downstream of the curtain following curtain deformation.

3. Additional instrumentation

Both upstream and downstream fields of view were offset (in the x direction) 19 mm from the centerline of the particle curtain, as shown in Fig. 3. Therefore, Schlieren imaging was also performed to visualize the direct interaction of the shock wave with the particle curtain. These measurements

were not performed simultaneously with the TR-PIV; however, due to repeatability, it was possible to synchronize the resulting Schlieren with the TR-PIV in postprocess.

The light source for the Schlieren was a Visual Instrumentation Corp. continuous-wave high-brightness LED (Model 900415). Two 101.6-mm-diameter planoconvex lenses, both with a focal length of 463.5 mm, were used. The first lens was used to collimate the light before entry into the test section. The secondary planoconvex lens focused light exiting the test section onto a vertical knife edge. Images were acquired using a Photron SA-Z camera, again with a resolution of 680×350 pixels, operating at a framing rate of 75 kHz, with a 105 mm camera lens.

Finally, pressure measurements were conducted using four PCB pressure sensors (Model 113B27). The PCB's have an output range of 0–6895 kPa, a resonant frequency greater than 500 kHz, and a sensitivity of ~ 7.25 mV/kPa. These sensors were installed along the ceiling, which collected time-resolved measurements sampled at a rate of 800 kHz. The sensors were located on either side of the curtain (two upstream and two downstream of the curtain), placed at $x = -82.4, -57.1, 31.7,$ and 57.1 mm, along the centerline. In addition, both the TR-PIV and Schlieren measurements were triggered off of a single PCB sensor (Model 113B26) located 0.5 m downstream of the fast-acting valve.

III. RESULTS AND DISCUSSION

Section III is divided into sections progressing towards estimation of the particle curtain drag. First, Schlieren images are presented in Sec. III A to give a brief overview of the curtain interaction. Following this, the TR-PIV measurements are discussed in Sec. III B. Finally, the TR-PIV measurements are used, in concert with unsteady pressure measurements, in Sec. III C to estimate the total integrated drag imposed on the curtain as a function of time. In all subsequent sections, unless otherwise specified, data are presented with time nondimensionalized as $t^* = tU_{\text{ind}}/\delta_0$, where U_{ind} is the induced velocity behind the initial shock wave.

A. Schlieren imaging of the curtain interaction

Schlieren imaging is presented in Fig. 6, highlighting particular features of the shock wave–particle curtain interaction. As many of the features of this interaction are common across all the three M_s and the two φ_p , only a single data set is shown here. These representative images correspond to the $M_s = 1.40$ shock wave impingement on the $\varphi_p = 9\%$ particle curtain. The field of view here encompasses 28 mm in the vertical direction (centered about mid-height) and 82 mm in the horizontal direction. Note that $t = 0$ s corresponds to the time at which the shock wave impinges on the front edge of the particle curtain.

The normal shock wave approaches the upstream side of the particle curtain at $t^* = -2.27$ [Fig. 6(a)]; due to the large disparity between the shock wave speed and the speed of the particles within the curtain (0.89 m/s), the particles appear to be frozen. In Fig. 6(b), the shock wave has now reached the particle curtain, resulting in the formation of a transmitted shock wave downstream of the curtain and a reflected shock wave that travels back upstream. Transmitted and reflected shock waves are characteristic of interactions with dense gas-solid mixtures and have been observed by a number of researchers previously [17–19,21].

The reflected shock wave moves slower than the transmitted shock wave in this example, as is clear from Figs. 6(c) and 6(d). However, for the case of $\varphi_p = 23\%$, it can be seen that the speeds of the two are much more comparable. A summary of the shock Mach numbers (obtained from measuring the time of arrival at the pressure transducers) can be seen in Table I. The uncertainties associated with each value represent a 95% confidence range.

For the case of $\varphi_p = 23\%$, the speed of the transmitted shock wave is, on average, 81.3% of the initial shock wave versus 82.0% for the reflected shock. Likewise, for $\varphi_p = 9\%$, these values are 93.0% and 81.3% for the transmitted and reflected shock waves, respectively. Over the range of

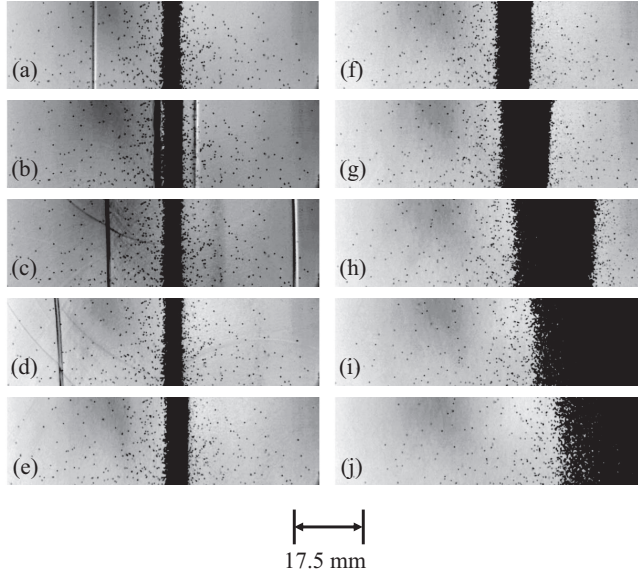


FIG. 6. Schlieren imaging of the $M_s = 1.40$ shock wave interaction with the $d_p = 300\text{--}355\ \mu\text{m}$ particle curtain: $t^* =$ (a) -2.27 , (b) 0.76 , (c) 3.78 , (d) 6.80 , (e) 12.85 , (f) 20.41 , (g) 27.96 , (h) 43.08 , (i) 58.20 , (j) 73.31 .

conditions tested herein, these results imply that the strengths of the reflected and transmitted shocks are more closely related to the initial volume fraction rather than the strength of the incident shock.

Referring to Eqs. (1) and (2), the particle curtain becomes more porous closer to the bottom of the test section owing to gravitational acceleration. Therefore, the reflected shock wave is stronger where the volume fraction is largest (at the top of the test section) and weaker where the volume fraction is smallest (at the bottom), resulting in the inclined shock wave evident in Fig. 6(d). Although not as readily apparent, the transmitted shock wave also is slightly inclined. It is expected that the change in curtain volume fraction as a function of height should induce two-dimensionalities within the gas phase upstream and downstream of the curtain, which will be explored in more detail in the following section.

In comparison to the experiments of Wagner *et al.* [11], the particle curtain shown here extends fully to the walls of the shock tube, whereas that of Wagner *et al.* [11] encompassed only 87% of the test section width. The result is that the transmitted shock wave here appears thinner and does not exhibit any apparent rippling associated with flow wrapping around the free edges of the curtain and shock diffraction. A contact surface issuing from the downstream edge of the particle curtain can briefly be seen in Fig. 6(c) between the particle curtain and the transmitted shock wave. This

TABLE I. Shock wave Mach numbers with percentage of M_s .

d_p (μm)	φ_p (%)	Initial	Transmitted	Reflected
106–125	23	1.22 ± 0.02	1.05 ± 0.03 (86.1%)	1.05 ± 0.01 (86.1%)
		1.40 ± 0.03	1.12 ± 0.02 (80.0%)	1.13 ± 0.01 (80.7%)
		1.45 ± 0.02	1.13 ± 0.03 (77.9%)	1.15 ± 0.03 (79.3%)
300–355	9	1.22 ± 0.02	1.16 ± 0.05 (95.1%)	1.04 ± 0.03 (85.2%)
		1.40 ± 0.03	1.29 ± 0.02 (92.1%)	1.13 ± 0.02 (77.9%)
		1.45 ± 0.02	1.33 ± 0.00 (91.7%)	1.17 ± 0.04 (80.7%)

contact surface is formed from the interface of the fluid downstream of the particle curtain and the fluid propagating through the curtain [21].

Deformation of the particle curtain is caused by a mismatch in the gas-phase velocities and pressures upstream and downstream of the curtain. As will be shown subsequently, the reflected shock wave decelerates the flow upstream of the particle curtain to a magnitude slower than that downstream of the curtain. This can be seen qualitatively, beginning in Fig. 6(e), where the downstream side of the curtain begins moving downstream itself. By Fig. 6(f), the upstream edge of the curtain has also begun to move in the streamwise direction, albeit at a slower rate.

Recall that the true volume fraction of the curtain (prior to impingement of the initial shock wave) contains a Gaussian distribution in the streamwise direction, with the maximum volume fraction centered at $x/\delta_0 = 0$, for $t \leq 0$. As was seen by Wagner *et al.* [20], as time increases, this absolute maximum is shifted downstream, resulting in a skewed distribution. Along with the streamwise widening of the particle curtain, the curtain volume fraction begins to decrease in time, creating a decreasing resistance to gas-phase flow. At $t^* = 27.96$ [Fig. 6(g)], this decreasing volume fraction is not readily apparent; however, beginning with $t^* = 43.08$ [Fig. 6(h)], light begins to penetrate through the upstream side of the curtain, implying a localized increase in porosity. The process continues at $t^* = 58.20$ and 73.31 [Figs. 6(i) and 6(j)], where further breakdown of the particle curtain results in increasing porosity becoming more evident within the upstream portion of the curtain.

B. Time-resolved PIV measurements of the flow upstream and downstream of the curtain

TR-PIV of the gas phase upstream and downstream of the particle curtain can provide further insight into (1) the unsteady drag on the curtain and (2) whether the height distribution of the curtain volume fraction could result in two-dimensionality within the gas phase.

Processed vector fields of the gas phase

Color contours of streamwise velocity (u) with in-plane streamlines at seven separate times are shown in Fig. 7 ($\varphi_p = 23\%$) and Fig. 8 ($\varphi_p = 9\%$), for $M_s = 1.40$. Here, the velocity fields are normalized by the induced velocity behind the initial shock, to facilitate comparison between upstream and downstream fields of view. White spaces within the vector fields correspond to either a lack of measured data or vectors that fall outside of the velocity threshold ($\pm \sim 0.5U_{\text{ind}}$). Because PIV was not possible at the location of the particle curtain (due to reflections from extraneous soda-lime particles), Schlieren imaging is added to Figs. 7 and 8 to show the motion of the shock waves between the two PIV fields of view. The flow features are generally the same for all three Mach numbers within a given particle size; therefore, only two of the six cases are shown.

As was described in Sec. III A, an initially planar shock wave can be seen approaching the particle curtain for $t^* < 0$ [Figs. 7(a), 7(b), 8(a), and 8(b)]. Once again, following arrival of the shock wave at the upstream edge of the curtain, reflected and transmitted shock waves are formed, each moving away from the curtain edges [Figs. 7(c) and 8(c)]. As the transmitted shock wave enters into the downstream field of view, the induced flow behind it initially appears rather steady in time (compared to later times), as seen in Figs. 7(d) and 8(d), respectively.

In comparing Fig. 7(e) with Fig. 8(e), it is readily apparent that the transmitted shock wave in the $\varphi_p = 23\%$ curtain is much weaker than in the $\varphi_p = 9\%$ curtain, given that the transmitted shock induces a slower flow downstream of the curtain. To better illustrate this, the resulting shock wave Mach numbers are shown in Table I. It should be pointed out here that evidence of an instability or nonuniformity is apparent within Fig. 7(e). This ‘‘dent,’’ which appears within the Schlieren images, appears to have been a random (i.e. nonrepeatable) occurrence and did not appear within the TR-PIV measurements. Furthermore, the analysis that follows in the later sections made use of the average of three runs; therefore, errors associated with the presence of such random nonuniformities are reflected in the uncertainty propagation that is performed in the later sections.

UNSTEADY DRAG FOLLOWING SHOCK WAVE . . .

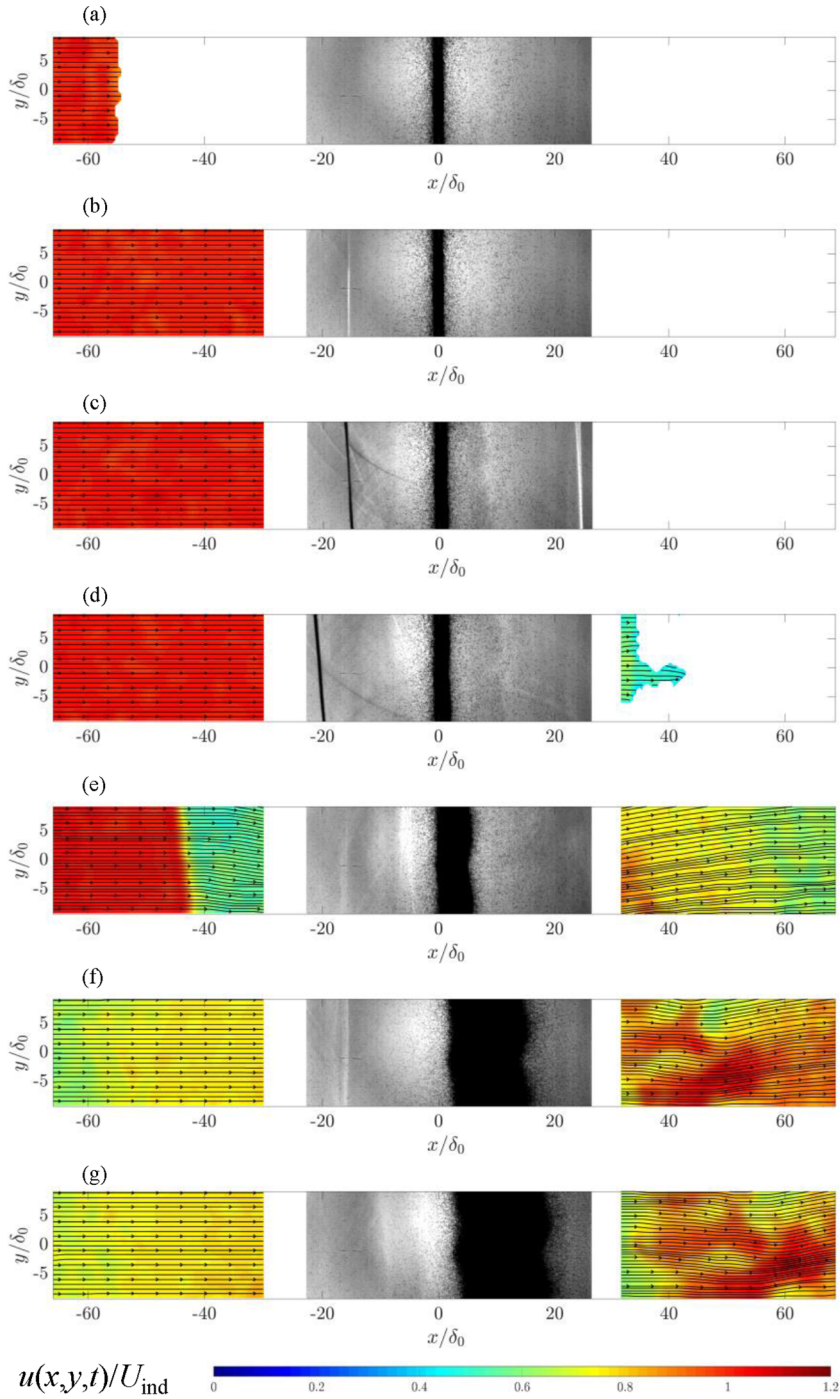


FIG. 7. TR-PIV color contours of (unsteady) streamwise velocity with in-plane streamlines for $M_s = 1.40$, $\varphi_p = 23\%$, upstream and downstream of the particle curtain, with associated Schlieren at $t^* =$ (a) -24.7 (-0.1867 ms), (b) -7.05 (-0.053 ms), (c) 10.60 (0.080 ms), (d) 14.10 (0.1067 ms), (e) 31.70 (0.240 ms), (f) 63.50 (0.480 ms), (g) 74.10 (0.560 ms).

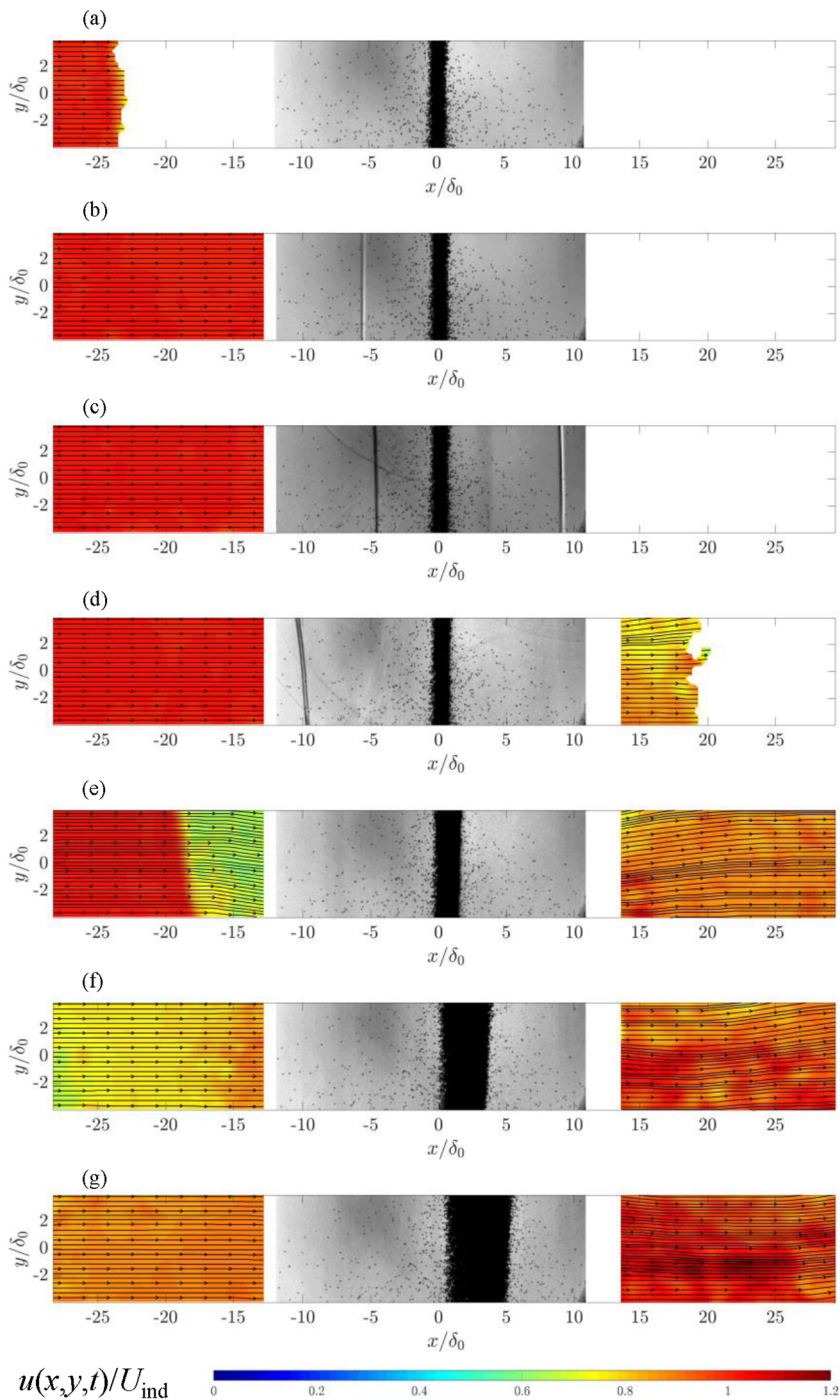


FIG. 8. TR-PIV color contours of (unsteady) streamwise velocity with in-plane streamlines for $M_s = 1.40$, $\varphi_p = 9\%$, upstream and downstream of the particle curtain, with associated Schlieren at $t^* =$ (a) -9.83 (-0.1733 ms), (b) -2.27 (-0.040 ms), (c) 3.78 (0.0667 ms), (d) 8.31 (0.1467 ms), (e) 15.87 (0.280 ms), (f) 27.96 (0.493 ms), (g) 35.52 (0.627 ms).

Once again, the transmitted and reflected shocks are both noticeably inclined. Interestingly, as is more evident in Figs. 7 and 8, the reflected shock wave becomes increasingly more inclined with increasing distance from the particle curtain. This is due to the stronger portions of the reflected shock (near the ceiling) traveling faster than the weaker portions (nearer the floor). The inclined reflected and transmitted shock waves imply that a small wall-normal velocity component should be generated within the gas-phase flows, as evidenced from the in-plane streamlines in Figs. 7(e), 7(f), 8(e), and 8(f). Importantly though, the relatively straight streamlines at most times in the figures suggest a relatively one-dimensional flow.

The reflected shock wave induces a wall-normal velocity directed towards the floor of the test section, upstream of the curtain. Similarly, a stronger positive wall-normal velocity is consistently formed downstream of the particle curtain, associated with the inclined transmitted shock wave. The wall-normal velocity appears transient, with the streamlines straightening out a time step or two later. This effect is especially clear within the upstream field of view.

In addition to the wall-normal velocity, an acceleration of the downstream induced flow, i.e., jetting through the particle curtain, is consistently seen [Figs. 7(e)–7(g) and Figs. 8(e)–8(g)]. This jetting is associated with acceleration of flow as it moves through the porous curtain. When the shock wave impinges on the particle curtain, the reflected shock, propagating back upstream, increases the pressure upstream of the particle curtain, while reducing the upstream gas-phase velocity. Downstream of the curtain, the pressure is lower in comparison to the upstream pressure (implied by larger velocities and by the presence of twice-shocked flow upstream of the curtain), resulting in a favorable pressure difference that accelerates flow through the curtain. The pressure difference that sets up across the curtain causes the curtain to spread, further reducing the volume fraction. Therefore, when jetting of flow through the curtain appears, it begins closer to the floor of the shock tube, where the volume fraction is initially the lowest, and gradually rises towards mid-height. If the volume fraction were perfectly uniform, then the flow would appear to uniformly accelerate. The occasional appearance of smaller velocities towards the floor can be attributed to random turbulent fluctuations and nonuniformities that may exist within the particle curtain.

Unsteadiness downstream of the particle curtain increases as a function of time, as shown in Figs. 7(e)–7(g) and Figs. 8(d)–8(g). One question that arises is whether or not this is a measure of small-scale unsteadiness induced by flow through the interstitial spacing within the curtain. Initially, the length scales associated with particle-induced turbulence are of the order of ~ 0.1 or 0.3 mm, depending on d_p . In contrast, the vector resolution of the data in Figs. 7 and 8 is ~ 0.8 mm; therefore, assuming the length scale of the largest turbulent eddy is of the order of d_p , these vector fields lack the spatial resolution necessary to properly resolve turbulent length scales less than or equal to the vector resolution.

This is only true within the initial transient. As time increases, turbulent length scales associated with the jetting grow within the downstream field of view as the curtain further deforms, creating larger interstitial spaces and allowing the resulting unsteadiness to begin to take shape within the processed vector fields. With increasing distance downstream of the curtain, these jets entrain flow from their surroundings and each other. Therefore, the jetting seen in Figs. 7(g) and 8(g) represent larger scale motions than particle-induced turbulence. On the other hand, if the interstitial spacing were to remain small, then the observed jetting would instead appear spatially uniform owing to limited spatial resolution inherent in the PIV measurements. The oblique view of the particle curtain shown in Fig. 2(a) indicates that some nonuniformity exists, which leads to small differences between individual runs; however, the conclusions presented here are drawn from multiple runs per test condition. Therefore, the conclusions should not be impacted by run-to-run differences.

Regarding three-dimensionalities within the particle curtain, spanwise-oriented TR-PIV was used to assess the spanwise dependency of the flow. An example of this is given in Fig. 9 for $M_s = 1.40$, $\varphi_p = 9\%$, where the vector field corresponds to a field of view downstream of the particle curtain, at $y/\delta_0 = 5.7$. Note that as this measurement is located above the field of view corresponding to Fig. 8, the velocities shown here are reduced owing to the higher volume fraction. Across the times shown, Fig. 9 indicates relatively little spanwise (z direction) dependency in the flow field downstream of

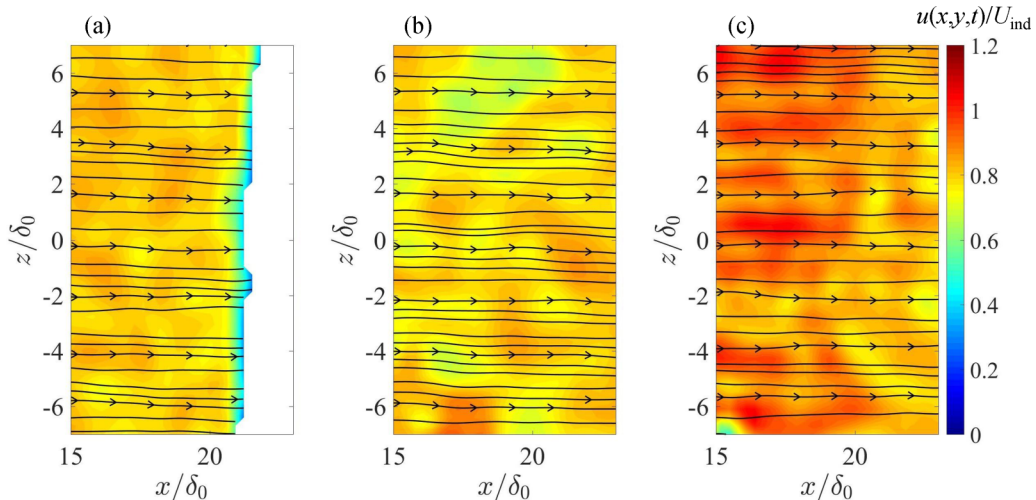


FIG. 9. TR-PIV color contours of (unsteady) streamwise velocity with in-plane streamlines downstream of the particle curtain for $M_s = 1.40$, $\varphi_p = 9\%$, taken in an $x - z$ oriented plane at $y/\delta_0 = 5.7$; $t^* =$ (a) 9.83 (0.173 ms), (b) 24.94 (0.440 ms), and (c) 40.1 (0.707 ms).

the curtain, although turbulent fluctuations appear to be present. As a result, the control volume analysis that is to follow will assume that there is a negligible spanwise influence on the flow.

C. Estimation of particle curtain total drag

1. Time traces of the unsteady measurements

The unsteady streamwise velocity (averaged across the height of the measurement domain) and the time-resolved pressure data upstream and downstream of the $\varphi_p = 9\%$ curtain at $x/\delta_0 = \pm 16.30$ are shown in Fig. 10 for the $M_s = 1.40$ case. For use in the subsequent calculations of the curtain drag, polynomials are fit to the unsteady data, as shown in Fig. 10 (linear for the velocity data and fifth order for the pressure data). These polynomials were used in order to facilitate a means of applying the analysis in the subsequent sections, namely, computing derivatives and matching values at given times. For the velocity term, it was assumed that the acceleration was nearly constant within the time frame of interest, as evidenced by Fig. 10(a). The curve fits were determined using unsteady data taken from three separate runs; for simplicity, they are presented here superimposed on time traces representing the average of these multiple runs. For the velocity data, this simplified operations such as taking time derivatives. The polynomial fits applied to the velocity data encompassed times corresponding to the passage of the reflected shock wave upstream of the curtain until just before the spreading of the particle curtain enters into the downstream field of view.

The pressure (P) curve fits were performed using a much longer length of time, to smooth out fluctuations and capture the overall unsteady trend to the pressure. As can be seen in the downstream pressure trace, the PCB registers increasing values, which reach a maximum around $t \approx 3$ ms. This increase in pressure is associated with passage of the bulk of the particle curtain. For this reason, along with limitations mentioned in the velocity data, the analysis was limited (in all cases) to $t < 1$ ms. Early in the upstream pressure trace, a series of (relatively) low frequency oscillations can be seen at $t < 2$ ms. These oscillations have not been incorporated into the analysis.

The transmitted shock is seen to reach the downstream sensor faster than the reflected shock reaches the upstream sensor, as can be seen in both Figs. 10(a) and 10(b). The TR-PIV measurements encompass a time span of $t < 2$ ms; it is clear from Fig. 10 that within this time, the pressure upstream

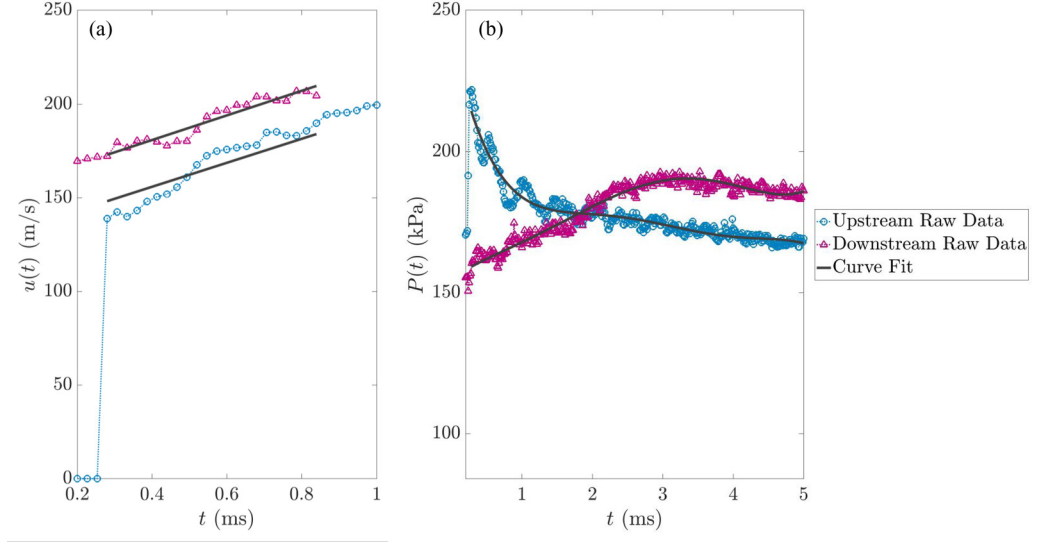


FIG. 10. Time traces and associated curve fits of the upstream and downstream (a) streamwise velocities (37.5 kHz) and (b) pressure taps (800 kHz), for $M_s = 1.40$, $\varphi_p = 9\%$. The time traces represent the average of three runs.

of the curtain is in fact larger than the pressure downstream, in agreement with the appearance of jetting evident in Figs. 7 and 8.

2. Control volume approach and derivation

A goal of this study was to resolve the unsteady drag (D) imposed on the particle curtain as a function of time. To do so, a control volume approach was used to estimate the total drag. A schematic of the control volume is provided in Fig. 11. The pressure sensors were placed at constant locations corresponding to $x/H = \pm 0.72$ along the top surface of the test section. The parameters entering the control volume were defined from the TR-PIV and the unsteady pressure measurements. Estimation of the unsteady drag was performed starting with the momentum equation. The streamwise momentum equation is

$$\Sigma F_x = [P_1(t) - P_2(t)]A_x - D(t) = \frac{\partial}{\partial t} \iiint \rho(t)u(t)dx dy dz + \iint \rho(t)u^2(t)dy dz. \quad (3)$$

Here, P is taken to be constant along the height of the test section. The first term on the right-hand side of Eq. (3) represents the rate change of momentum within the control volume, whereas the second term on the right-hand side represents the flux of momentum across the boundaries of the control volume. The cross-sectional area A_x is defined here as $\Delta z H$. For simplicity, unsteady terms will be implied for the remainder of the derivation, i.e., $D \equiv D(t)$.

Integrating Eq. (3) results in

$$D = (P_1 - P_2)A_x + (\rho_1 u_1^2 - \rho_2 u_2^2)A_x - \frac{\partial}{\partial t} \iiint \rho u dx dy dz. \quad (4)$$

Equation (4) can be simplified further if u is assumed constant across the height of the test section (i.e., an average value) in order to reduce the noise within the measurement. In addition, a functional form of ρu is necessary to solve the remaining integral. This is done by assuming a linear relationship

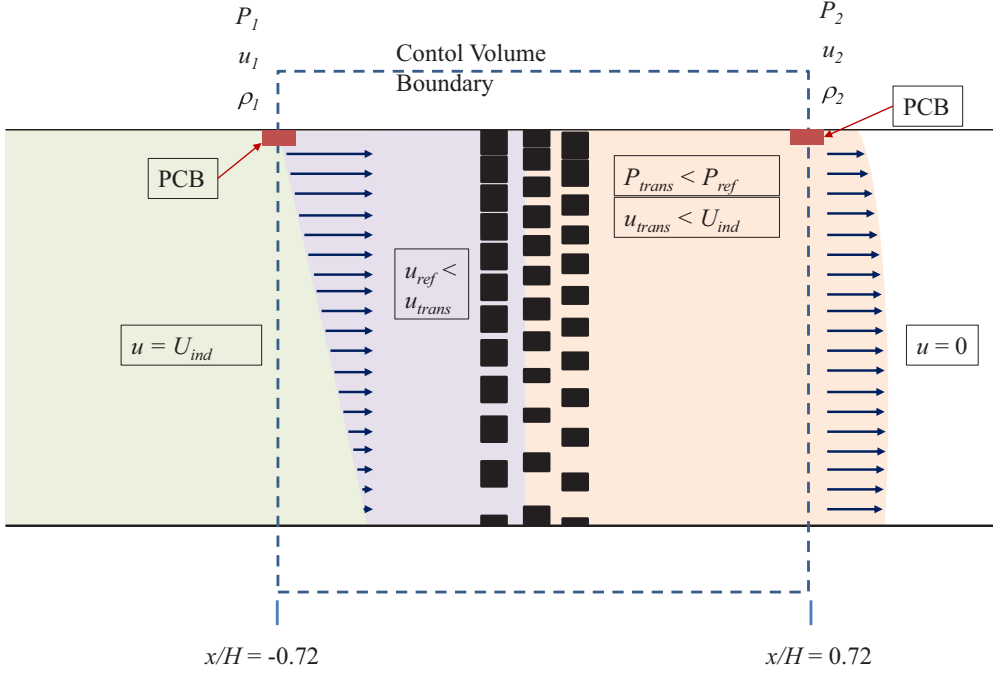


FIG. 11. Schematic of the control volume method.

for ρu :

$$\frac{\partial}{\partial t} \iiint \rho u dx dy dz = A_x \frac{\partial}{\partial t} \int \rho u dx \approx A_x \frac{\partial}{\partial t} \int \left[\frac{\rho_2 u_2 - \rho_1 u_1}{\Delta x} (x - x_1) + \rho_1 u_1 \right] dx.$$

Further simplification results in

$$D = A_x \left[(P_1 - P_2) + (\rho_1 u_1^2 - \rho_2 u_2^2) - \frac{\Delta x}{2} \frac{\partial}{\partial t} (\rho_1 u_1 + \rho_2 u_2) \right]. \quad (5)$$

The previous measurements have shown that the induced flow fields upstream and downstream of the particle curtain are, in fact, two dimensional; however, since the flows are streamwise dominated, the use of Eq. (5) should provide a reasonable estimate of the unsteady drag.

The terms in Eq. (5) represent the change in momentum and pressure across the particle curtain. The pressure difference across the boundaries of the control volume is given by

$$(P_1 - P_2)A_x = \Delta P A_x.$$

Likewise, the difference in momentum flux across the same boundaries is

$$(\rho_1 u_1^2 - \rho_2 u_2^2)A_x = \Delta(\rho u^2)A_x.$$

Finally, the change in momentum within the control volume as a function of time is

$$\frac{\Delta x A_x}{2} \frac{\partial}{\partial t} (\rho_1 u_1 + \rho_2 u_2) = \frac{\partial(\rho u)}{\partial t} \Delta x A_x.$$

To solve Eq. (5), it is necessary to have measurements of the pressure upstream and downstream of the curtain, along with the corresponding densities (two thermodynamic state variables). With regards to the pressure measurements, the curve fits of Fig. 10 were used to provide interpolated values at time steps that corresponded with TR-PIV measurements.

After the initial shock wave has passed, a series of compression waves propagate downstream; likewise, an expansion fan also moves upstream [21], resulting in changes to both the pressure and the fluid density upstream and downstream of the curtain, as a function of time. To estimate these changes to the fluid density, an isentropic relationship was used,

$$\frac{\rho(t + \Delta t)}{\rho(t)} = \left[\frac{P(t + \Delta t)}{P(t)} \right]^{(1/\gamma)}. \quad (6)$$

Here, γ is taken to be the ratio of specific heats. In applying Eq. (6), it is assumed that the postshock flows are relatively adiabatic and that the compression and expansion processes are reversible; therefore, this equation represents an idealized estimation of the density derived from the unsteady pressure measurements assuming isentropic conditions.

Note that this is an estimate of the true unsteady density distribution as a function of time, where an incompressible assumption would not be valid. Furthermore, it was assumed that although the interaction with the particle curtain is not without losses, the changes to the density associated with expansion and compression waves emanating from the particle curtain are nearly isentropic processes at these modest Mach numbers. In addition to the use of Eq. (6), the initial value of the density was determined from the isentropic compressible flow equations, following determination of the reflected or transmitted shock wave Mach numbers.

3. Calculation of total drag

The resulting drag on the curtain, in both dimensional and nondimensional forms, is shown in Fig. 12 for $M_s = 1.22, 1.40,$ and 1.45 . Uncertainty bars have been added to the curves to display the estimated precision and bias errors of the drag calculations.

The precision errors were estimated by performing a propagation of uncertainty analysis on each drag curve, assuming errors associated with scatter within experimental data, along with error in the curve-fitting process. The standard deviations associated with each curve fit were defined using

$$\epsilon_{\xi} = \sqrt{\frac{\sum(\xi_i - \xi_{fi})^2}{\nu}}, \quad (7)$$

where ξ_i represents the raw data points, ξ_{fi} is the curve fit, and ν is the degrees of freedom for each curve fit [38].

The primary source of bias uncertainty stems from the use of pressure sensors at the top of the measurement volume. The inclined shocks that emanate from the curtain, particularly those upstream, suggest a pressure difference across the height of the test section to exist at least at early interaction times. From the shock angles shown in Figs. 7 and 8, this bias uncertainty is estimated to be about 3% of a given pressure value. The potential error associated with this discrepancy is small compared to the magnitude of the contribution of the pressure compared to the other drag components. Therefore, the conclusions associated with this analysis are not impacted by this bias uncertainty.

The combined bias and precision uncertainties of each parameter are listed in Table II. Propagation of the bias uncertainties, along with the precision uncertainties, was carried out according to

$$\epsilon_D = \sqrt{\sum \left(\epsilon_{\xi_j} \frac{\partial D}{\partial \xi_j} \right)^2 + \left(\epsilon_{b,P} \frac{\partial D}{\partial P} \right)^2 + \left(\epsilon_{b,u} \frac{\partial D}{\partial u} \right)^2}, \quad (8)$$

where $\epsilon_{b,P}$ and $\epsilon_{b,u}$ represent the bias uncertainties and ϵ_D represents the total uncertainty in the drag [38]. The uncertainty bars shown in Fig. 12 represent standard error values, i.e., $\pm \epsilon_D / \sqrt{3}$, where 3 is the number of independent runs performed. Therefore, these drag estimates are presented within 68% confidence.

As seen in Fig. 12(a), the drag in each case starts out at an initially large value that rapidly asymptotes towards what appears to be a constant value as the fluid properties and velocities

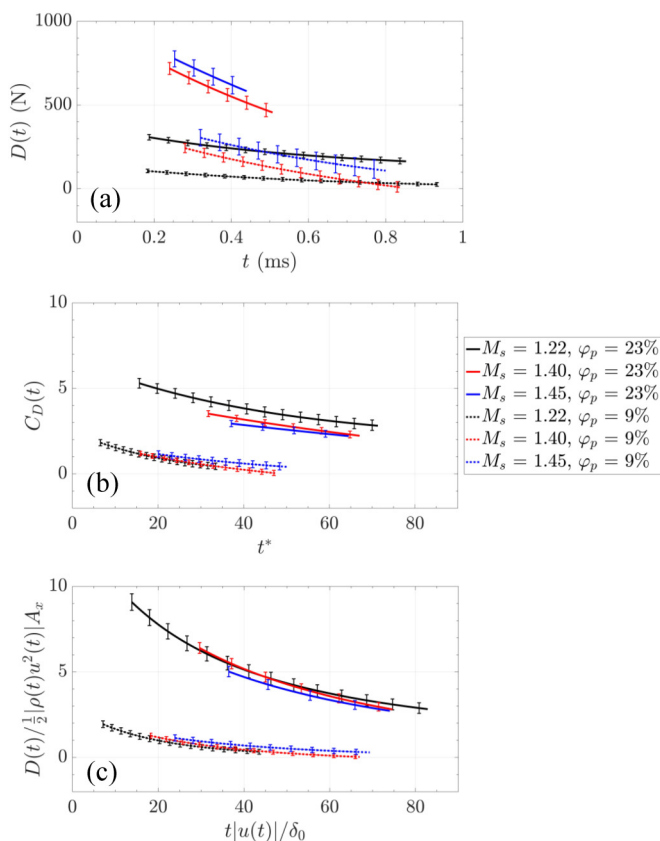


FIG. 12. (a) Estimation for the change in drag as a function of time. (b) Same as (a), but with values nondimensionalized by induced values behind the initial shock wave. (c) Values nondimensionalized by the average of unsteady values on either side of the curtain.

equilibrate on either side of the curtain. For the cases corresponding to $\varphi_p = 9\%$, the drag can be seen to approach zero (within the uncertainty of the error bars). As M_s increases, the difference between the drag curves for the two volume fractions increases. Additionally, the uncertainty bars on the drag curves increase with both volume fraction and M_s .

In addition to the dimensional quantities of Fig. 12(a), Fig. 12(b) displays the same drag information presented in a nondimensionalized form. Normalization was carried out using values of velocity and density corresponding to the passage of the initial shock, defining the coefficient of

TABLE II. Uncertainties (ϵ_{ξ_j}) associated with velocity, pressure, and density.

d_p (μm)	M_s	ϵ_{u_1} (m/s)	ϵ_{u_2} (m/s)	ϵ_{p_1} (kPa)	ϵ_{p_2} (kPa)	ϵ_{ρ_1} (kg/m ³)	ϵ_{ρ_2} (kg/m ³)
106–125	1.22	6.7	8.6	3.4	2.0	0.04	0.05
	1.40	13.8	13.0	4.9	3.9	0.05	0.03
	1.45	9.9	10.7	6.1	5.4	0.23	0.07
300–355	1.22	3.0	3.8	1.8	1.8	0.02	0.02
	1.40	7.6	6.4	3.5	3.3	0.03	0.05
	1.45	9.2	13.1	4.4	6.9	0.05	0.03

drag, $C_D = D/\frac{1}{2}\rho_{\text{ind}}U_{\text{ind}}^2A_x$. The values of density and velocity behind the initial shock wave were chosen for nondimensionalization, as they are useful as predictable quantities from theory, rather than quantities that require measurement of each flow field.

Comparing Figs. 12(a) and 12(b), the three drag curves for each volume fraction appear to nearly collapse when nondimensionalized [relative to the disparate trends in Fig. 12(a)]. The effect of volume fraction is most apparent in this nondimensional form from the offset that exists between the $\varphi_p = 23\%$ and 9% cases. Here, the larger values of C_D are associated with the higher volume fraction. In these data, the volume fraction of the particle curtain was a function of the size of the particles used. Therefore, it is not possible with this data set to decouple the influence of the particle size from that associated with the volume fraction.

In addition to the nondimensionalization presented in Fig. 12(b), Fig. 12(c) restates the drag data, with time and drag normalized by the average of the unsteady flow conditions on either side of the particle curtain, i.e.,

$$|\rho(t)u^2(t)| = \sqrt{[\rho_1(t)u_1^2(t)]^2 + [\rho_2(t)u_2^2(t)]^2} \quad (9)$$

and

$$|u(t)| = \sqrt{[u_1(t)]^2 + [u_2(t)]^2}, \quad (10)$$

where the subscripts 1 and 2 refer to upstream and downstream of the curtain, respectively. Using the unsteady values of velocity and density, the collapse of the drag curves appears to be more significant than using the shock-induced values of Fig. 12(b). Once again, the effect of φ_p can be seen from the offset apparent between the two sets of drag curves, along with the trend of the drag decreasing with increasing time. While this normalization appears to arrive at a more complete collapse of the data, its usefulness is limited in that knowledge of the change in flow conditions with time is necessary for implementation.

It is important to point out that the drag shown here exhibits prolonged unsteadiness in comparison to the dilute mixture drag measurements shown by Parmar *et al.* [10]. The dilute drag was shown to have unsteadiness that appeared to rapidly approach quasisteady values following passage of the initial shock wave. In comparison, the drag shown from this data set is much more prolonged, in agreement with Ling *et al.* [21]. However, as the drag estimates were obtained after the passage of the reflected shock wave, these data were not able to resolve the initial transient spike in drag [21].

4. Contributions to drag

In order to appreciate the contribution of each of the terms of Eq. (5), Figs. 13 and 14 show the components of drag as a function of time for the three Mach numbers, for $\varphi_p = 23\%$ and $\varphi_p = 9\%$ cases, respectively. Note that the two higher Mach number cases ($M_s = 1.40, 1.45$) for $\varphi_p = 23\%$ [Figs. 13(b) and 13(c)] truncate much earlier than their $\varphi_p = 9\%$ counterparts; the velocity and pressure data were truncated at the point in time when a large number of particles began to enter the downstream field of view. For the $\varphi_p = 23\%$ particle curtain, this happened much earlier than for $\varphi_p = 9\%$.

In each case, trends appear to approach zero with increasing time, again due to conditions on either side of the curtain equalizing as the curtain deforms. In the case of $M_s = 1.22$ [Figs. 13(a) and 14(a)], the change in momentum flux and rate change of momentum terms both appear to reach nearly zero values relatively early, compared to the other two Mach numbers. In this case, the drag appears to be almost wholly associated with the pressure drop across the curtain.

In comparison to $M_s = 1.22$, the remaining two Mach numbers [$M_s = 1.40, 1.45$; Figs. 13(b), 13(c), 14(b), and 14(c)] behave much more similarly. In these instances, both the momentum flux and rate change of momentum terms are non-negligible. As time increases, the rate change of momentum within the control volume approaches zero from initially large positive values. In contrast, the change of momentum flux increases rapidly towards zero. In agreement with the $M_s = 1.22$ case [Figs. 13(a)

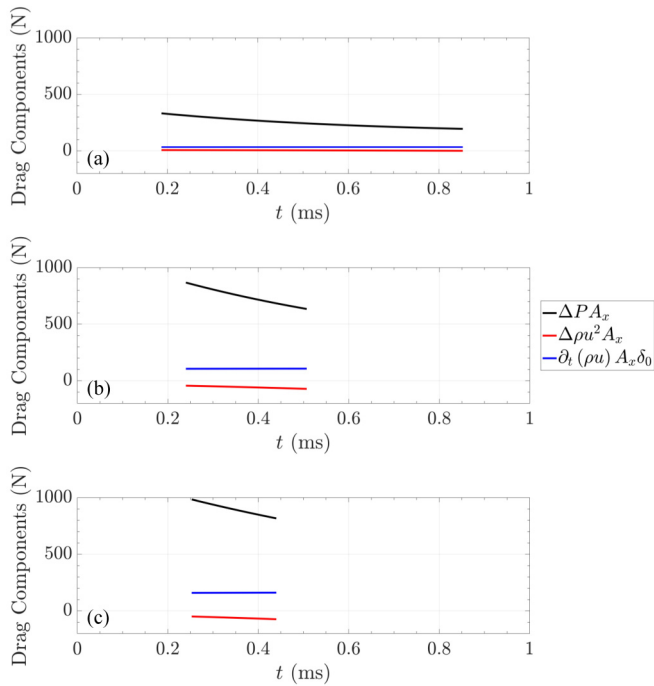


FIG. 13. The three components of drag (as a function of time) for $\varphi_p = 23\%$, $M_s =$ (a) 1.22, (b) 1.40, (c) 1.45.

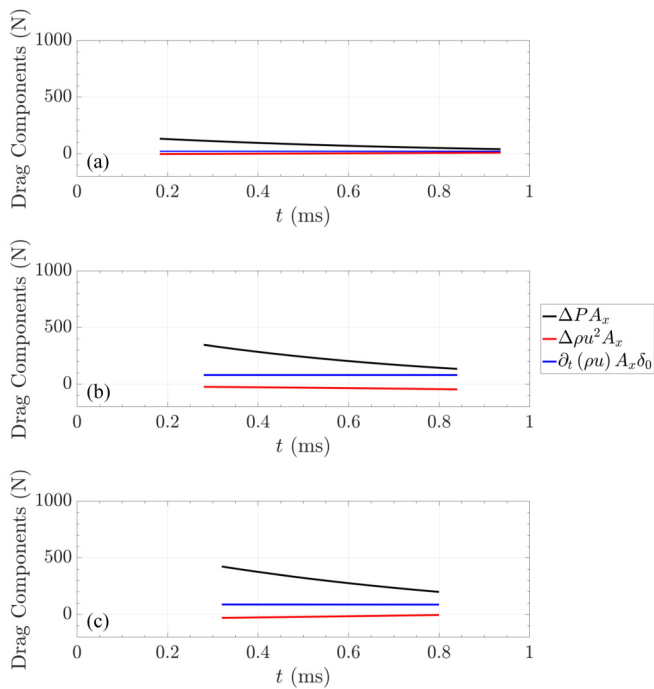


FIG. 14. The three components of drag (as a function of time) for $\varphi_p = 9\%$, $M_s =$ (a) 1.22, (b) 1.40, (c) 1.45.

TABLE III. Percent contribution of $A_x \Delta x \partial(\rho u) / \partial t$ at beginning of curve.

φ_p (%)	M_s	$A_x \Delta x \partial(\rho u) / \partial t$ (%)
23	1.22	10.4
	1.40	14.7
	1.45	20.5
9	1.22	22.4
	1.40	33.1
	1.45	28.9

and 14(a)], these Mach numbers both indicate that the largest contributor to the total drag is the pressure difference. This is in agreement with Theofanous *et al.* [26], who showed that the trajectory of the particle curtain appeared to be governed by the pressure difference.

As a result of the data shown here, determination of the curtain drag based solely on pressure information appears to provide an overestimate. This is in agreement with Ling *et al.* [21], whose results stated that the pressure gradient within the curtain was not sufficient for estimation of the curtain drag. With increasing M_s , the contribution of the rate change of the momentum within the control volume to the total drag becomes larger. An example of this is shown in Table III, which gives the percent contribution of this term at the start of each drag curve. As evident, the percentage contribution of this term can also be seen to increase with *decreasing* φ_p .

Regarding the inverse relationship between φ_p and the percentage contributions seen in Table III, the reason for this can be determined from Figs. 13 and 14. For $\varphi_p = 9\%$, the pressure difference across the curtain is less severe than for $\varphi_p = 23\%$, as lower volume fractions present a reduced flow resistance. In contrast, the pressure differences seen for $\varphi_p = 23\%$ are much greater, providing a larger contribution to the total drag. As to the growth in the importance of rate change of momentum within the control volume with M_s , this term is proportional to the rate of change in the gas-phase density. The direct relationship with this term, as seen in Table III, indicates a (logical) growing importance of compressibility effects with M_s .

IV. CONCLUSIONS

Experiments were conducted using TR-PIV with a pulse-burst laser and high-speed pressure sensors to make time-resolved measurements of the gas-phase velocity upstream and downstream of a particle curtain following impingement by a shock wave. These measurements provided the data necessary for estimating the unsteady drag imposed on the particle curtain immediately following the shock wave interaction. The particle curtain was formed from soda-lime particles free falling through a 3.2 mm slit, resulting in a curtain with a volume fraction of 23% or 9% at mid-height, depending on the particle diameter. Three separate tests of the shock wave–particle curtain interaction were measured, at shock Mach numbers corresponding to $M_s = 1.22, 1.40$, and 1.45. In addition, time-resolved pressure measurements made upstream and downstream of the particle curtain allowed for the determination of the total drag on the curtain as a function of time.

When the initial shock wave impinged on the particle curtain, an upstream-propagating reflected shock wave and a downstream-propagating transmitted shock wave were created, which altered the pressures on either side of the curtain. The variation of the particle curtain volume fraction as a function of height caused the reflected shock wave to be inclined away from the particle curtain, whereas the transmitted shock wave was slightly inclined back towards the curtain, leading to the formation of two-dimensionality within the respective induced gas-phase velocity fields.

The pressure difference between the upstream and downstream sides of the curtain accelerated flow through the curtain, resulting in an increase in downstream gas-phase velocity. This was accompanied by a jetting of flow through the interstitial spaces of the curtain that could be seen

downstream of the curtain once the curtain began to deform. Furthermore, as time increased, the pressure difference across the curtain decreased, which is the source of the long-term unsteady drag in dense gas-solid mixtures.

Estimation of the unsteady particle curtain drag was accomplished using a control volume approach. It was observed that the favorable pressure difference established by the reflected or transmitted shock waves is the dominant drag term, consistent with the conclusions of Theofanous *et al.* [26]. Upon normalization, the data appeared to approach a similar trend, decreasing with increasing time as conditions on either side of the curtain equalize. The data here agree in many regards with the work by Ling *et al.* [21], who showed a prolonged unsteadiness within the particle curtain drag, in comparison to that observed within dilute gas-solid mixtures. It is seen that in the case of the two volume fractions tested, the drag is a function of volume fraction.

ACKNOWLEDGMENTS

The authors would like to thank Thomas W. Grasser for his help designing the experimental hardware and Dr. Lawrence DeChant for his help in the control volume analysis. This work is supported by Sandia National Laboratories and the U.S. Department of Energy. Sandia National Laboratories is a multiprogram laboratory managed and operated by the Sandia Corporation, a wholly owned subsidiary of the Lockheed Martin Corporation, for the U.S. Department of Energy's National Nuclear Security Administration, under contract DE-AC04-94AL85000.

-
- [1] E. J. Chang and K. Kailasanath, Shock wave interactions with particles and liquid fuel droplets, *Shock Waves* **12**, 333 (2003).
 - [2] B. Vessiere, Detonations in gas-particle mixtures, *J. Propul. Power* **22**, 1269 (2006).
 - [3] W. Merzkirch and K. Bracht, The erosion of dust by a shock wave in air: Initial stages with laminar flow, *Int. J. Multiphas. Flow* **4**, 89 (1978).
 - [4] S. L. Davis, T. B. Dittmann, G. B. Jacobs, and W. S. Don, Dispersion of a cloud of particles by a moving shock: Effects of the shape, angle of rotation, and aspect ratio, *J. Appl. Mech. Tech. Phys.* **54**, 900 (2013).
 - [5] F. Zhang, D. L. Frost, P. A. Thibault, and S. B. Murray, Explosive dispersal of solid particles, *Shock Waves* **10**, 431 (2001).
 - [6] G. Rudinger, Some properties of shock relaxation in gas flows carrying small particles, *Phys. Fluids* **7**, 658 (1964).
 - [7] F. E. Marble, Dynamics of dusty gases, *Annu. Rev. Fluid Mech.* **2**, 397 (1970).
 - [8] M. Sommerfeld, The unsteadiness of shock waves propagating through gas-particle mixtures, *Exp. Fluids* **3**, 197 (1985).
 - [9] J. Magnaudet and I. Eames, The motion of high-Reynolds number bubbles in inhomogeneous flows, *Annu. Rev. Fluid Mech.* **32**, 659 (2000).
 - [10] M. Parmar, A. Haselbacher, and S. Balachandar, Modeling of the unsteady force for shock-particle interaction, *Shock Waves* **19**, 317 (2009).
 - [11] J. L. Wagner, S. J. Beresh, S. P. Kearney, B. O. M. Pruett, and E. K. Wright, Shock tube investigation of quasi-steady drag in shock-particle interactions, *Phys. Fluids* **24**, 123301 (2012).
 - [12] M. Sun, T. Saito, K. Takayama, and H. Tanno, Unsteady drag on a sphere by shock wave loading, *Shock Waves* **14**, 3 (2004).
 - [13] E. Loth, Compressibility and rarefaction effects on drag of a spherical particle, *AIAA J.* **46**, 2219 (2008).
 - [14] A. A. Martinez, G. C. Orlicz, and K. P. Prestridge, A new experiment to measure shocked particle drag using multi-pulse particle image velocimetry and particle tracking, *Exp. Fluids* **56**, 1 (2015).
 - [15] A. Britan, T. Elperin, O. Igra, and J. P. Jiang, Acceleration of a sphere behind planar shock waves, *Exp. Fluids* **20**, 84 (1995).

- [16] B. W. Skews, M. S. Bredin, and M. Efuno, Drag measurements in unsteady compressible flow. Part 2: Shock wave loading of spheres and cones, *R&D J. South Afr. Inst. Mech. Eng.* **23**, 13 (2007).
- [17] V. M. Boiko, V. P. Kiselev, S. P. Kiselev, A. N. Papyrin, S. V. Poplavsky, and V. M. Formin, Shock wave interaction with a cloud of particles, *Shock Waves* **7**, 275 (1997).
- [18] X. Rogue, G. Rodriguez, J. F. Haas, and R. Saurel, Experimental and numerical investigation of the shock-induced fluidization of a particles bed, *Shock Waves* **8**, 29 (1998).
- [19] J. L. Wagner, S. J. Beresh, S. P. Kearney, W. M. Trott, J. N. Castaneda, B. O. Pruett, and M. R. Baer, A multiphase shock tube for shock wave interactions with dense particle fields, *Exp. Fluids* **52**, 1507 (2012).
- [20] J. L. Wagner, S. P. Kearney, S. J. Beresh, E. P. DeMauro, and B. O. Pruett, Flash x-ray measurements on the shock-induced dispersal of a dense particle curtain, *Exp. Fluids* **56**, 1 (2015).
- [21] Y. Ling, J. L. Wagner, S. J. Beresh, S. P. Kearney, and S. Balachandar, Interaction of a planar shock wave with a dense particle curtain: Modeling and experiments, *Phys. Fluids* **24**, 113301 (2012).
- [22] J. D. Regele, J. Rabinovitch, T. Colonius, and G. Blanquart, Unsteady effects in dense, high speed, particle laden flows, *Multiphas. Flow* **61**, 1 (2014).
- [23] H. Liu, Y. Guo, and W. Lin, Simulation of shock-powder interaction using kinetic theory of granular flow, *Powder Technol.* **273**, 133 (2015).
- [24] R. W. Houim and E. S. Oran, A multiphase model for compressible granular-gaseous flows: Formulation and initial tests, *J. Fluid Mech.* **789**, 166 (2016).
- [25] M. Kellenberger, C. Johansen, G. Ciccarelli, and F. Zhang, Dense particle cloud dispersion by a shock wave, *Shock Waves* **23**, 415 (2013).
- [26] T. G. Theofanous, V. Mitkin, and C. H. Chang, The dynamics of dense particle clouds subjected to shock waves. Part 1. Experiments and scaling laws, *J. Fluid Mech.* **792**, 658 (2016).
- [27] J. L. Wagner, S. J. Beresh, E. P. DeMauro, K. M. Casper, D. R. Guildenbecher, B. O. Pruett, and P. Farias, Pulse-burst PIV measurements of transient phenomena in a shock tube, *AIAA* (2016), doi:10.2514/6.2016-0791.
- [28] R. J. Goetsch and J. D. Regele, Discrete element method prediction of particle curtain properties, *Chem. Eng. Sci.* **137**, 852 (2015).
- [29] J. H. Arakeri, D. Das, A. Krothapalli, and L. Lourenco, Vortex ring formation at the open end of a shock tube: A particle image velocimetry study, *Phys. Fluids* **16**, 1008 (2004).
- [30] K. Prestridge, P. M. Rightley, P. Vorobieff, R. F. Benjamin, and N. A. Kurnit, Simultaneous density-field visualization and PIV of a shock-accelerated gas curtain, *Exp. Fluids* **29**, 339 (2000).
- [31] K. Prestridge, P. Vorobieff, P. M. Rightley, and R. F. Benjamin, Validation of an Instability Growth Model Using Particle Image Velocimetry Measurements, *Phys. Rev. Lett.* **84**, 4353 (2000).
- [32] N. Haehn, C. Weber, J. Oakley, M. Anderson, D. Ranjan, and R. Bonazza, Experimental investigation of a twice-shocked spherical gas inhomogeneity with particle image velocimetry, *Shock Waves* **21**, 225 (2011).
- [33] S. J. Beresh, S. P. Kearney, J. L. Wagner, D. R. Guildenbecher, J. F. Henfling, R. W. Spillers, B. O. M. Pruett, N. Jiang, M. N. Slipchenko, J. Mance, and S. Roy, Pulse-burst PIV in a high-speed wind tunnel, *Meas. Sci. Technol.* **26**, 095305 (2015).
- [34] M. Samimy and S. K. Lele, Motion of particles with inertia in a compressible free shear layer, *Phys. Fluids* **3**, 1915 (1991).
- [35] S. W. Smith, *Digital Signal Processing*, 2nd ed. (California Technical, San Diego, CA, 1999).
- [36] Y. Murai, Y. Oishi, Y. Takeda, and F. Yamamoto, Turbulent shear stress profiles in a bubbly channel flow assessed by particle tracking velocimetry, *Exp. Fluids* **41**, 343 (2006).
- [37] W. Zhang, Y. Wang, and S. J. Lee, Simultaneous PIV and PTV measurements of wind and sand particle velocities, *Exp. Fluids* **45**, 241 (2008).
- [38] R. S. Figliola and D. E. Beasley, Probability and statistics, in *Theory and Design for Mechanical Measurements*, 3rd ed. (Wiley, New York, 2004), pp. 109–148.